Macromolecules

pubs.acs.org/Macromolecules

Article

Designing Actuation in pH-Responsive Hydrogels

Jiaxing Yuan and Tine Curk*

Cite This: *Macromolecules* 2026, 59, 939−949

ABSTRACT: Polyelectrolyte hydrogels can reversibly swell and shrink in response to environmental stimuli such as pH and temperature, making them useful as smart materials with tunable properties. However, their application has been limited by slow response time and low power density. Here, we employ hybrid molecular dynamics and Monte Carlo simulations to investigate the actuation behavior of pH-responsive nanogels, explicitly accounting for dynamic protonation and hydrodynamic interactions. We find that polyelectrolyte hydrogels exhibit a closed-loop phase behavior bounded by two critical points. Near a critical point, nanogels undergo conformational switching on a microsecond time scale and generate work densities of approximately 10^5 J/m^3, exceeding those of skeletal muscles. Importantly, the power density scales as L^{-2}, where L is the linear size of the gel. This suggests that high-performance actuators can be realized by keeping L small, for example, by stacking nanoscale gel components. These results establish a fundamental connection between microscopic structure and dynamic response, and offer quantitative guidelines for designing responsive hydrogels.

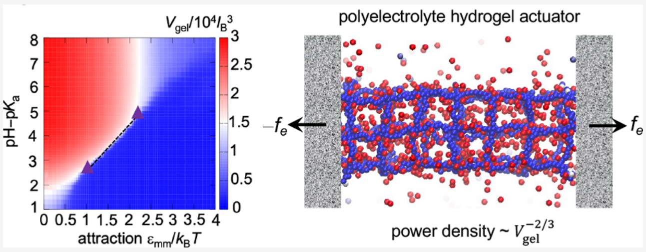

■ INTRODUCTION

Polyelectrolyte (PE) hydrogels are three-dimensional networks of cross-linked charged polymers with widespread industrial applications.[1,2] Their ability to undergo large, reversible conformational changes in response to environmental cues, such as temperature,[3−6] pH,[7−9] salt concentration,[10,11] and electric or magnetic fields,[12] makes them ideal components for smart materials and devices, including drug delivery systems[7] and soft robotic actuators.[13,14] By incorporating stimuli-responsive elements such as ionizable groups, hydrogels can undergo controlled deformations and perform mechanical work.[15] A fundamental understanding of both the thermodynamics and kinetics of the swelling−collapse transition is required to rationally design conformational response and efficient actuation in hydrogels.

Many hydrogels function as weak acids or bases, with a charge state that depends on conformation via the charge regulation (CR) effect.[16−20] This coupling can lead to a discontinuous swelling−collapse transition.[21,22] While the equilibrium phase behavior of PE hydrogels has been extensively studied using theory,[17,22,23] simulations[19,24−29] and experiments,[21,30−34] much less is known about their response kinetics,[30,35] particularly in nanogels where time-resolved measurements of nanoscale conformational changes remain experimentally challenging.[36,37] Nanogels, with their large surface-to-volume ratios[38,39] and fast dynamic responses,[37,40] are especially promising for biomedical and nanoengineering applications such as controlled drug delivery and miniaturized actuators. Despite their potential, the full pH−temperature phase diagram, dynamic response, and power output of pH-responsive hydrogels remain incompletely understood, especially with regard to the role of hydrodynamics. In particular, current hydrogel-based actuators suffer from slow response and low power density, which is orders of magnitude smaller than that of skeletal muscles.[41]

In this work, we study the coupling between charge, structure, and hydrodynamics in a polyelectrolyte nanogel. Using hybrid molecular dynamics (MD) and Monte Carlo (MC) simulations, combined with analytical theory, we investigate equilibrium conformations and collapse−expansion dynamics, and uncover fundamental trade-offs among work, power, and hysteresis. We demonstrate that the interplay of electrostatics, hydrodynamics, and polymer elasticity enables efficient chemical-to-mechanical energy conversion in pH-driven actuation, and derive design principles for optimizing the actuation performance of hydrogels.

Modeling pH-driven actuation requires accurate treatment of both dynamic protonation and hydrodynamic interactions (HI). We use a coarse-grained model in which all charges and ionizable sites are explicitly represented, capturing the interplay among protonation, gel conformation, electrostatics, counterion osmotic pressure, and excluded volume effects. The gel consists of bead−spring chains with cross-linking distance N_p

Received: December 2, 2025
Revised: January 6, 2026
Accepted: January 9, 2026
Published: January 15, 2026

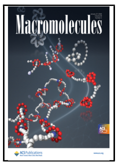

https://doi.org/10.1021/acs.macromol.5c03370

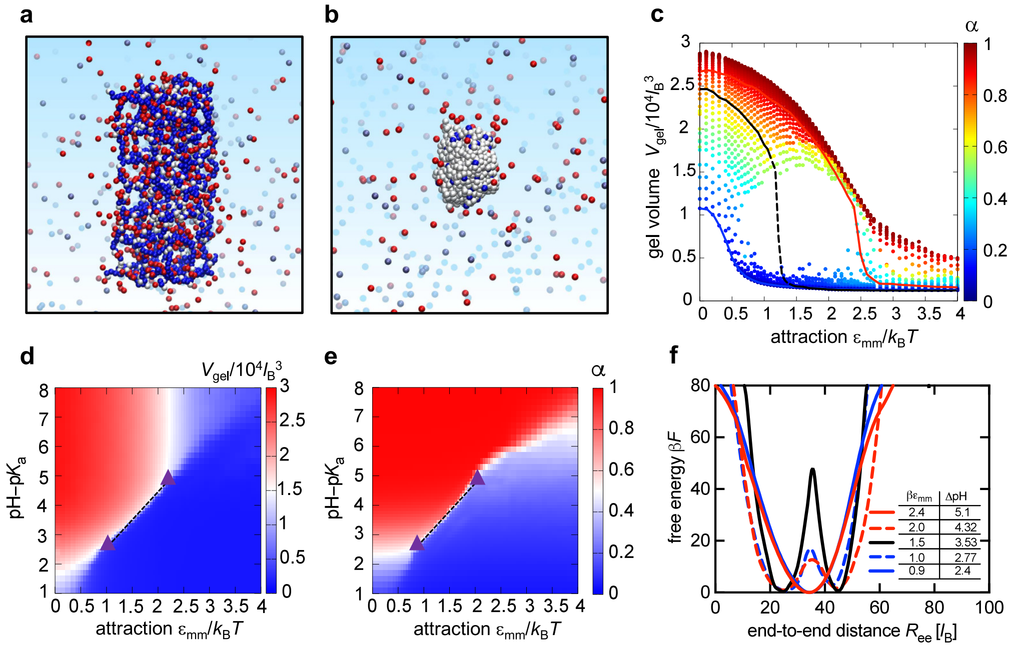

Figure 1. Equilibrium phase diagram of a nanogel. (a, b) Representative conformations of the expanded (pH − pK_a = 6) and collapsed (pH − pK_a = 1) states at $\varepsilon_{mm} = k_BT$, showing charged (blue) and neutral (white) monomers, free cations (red), and anions (metallic blue). (c) Average gel volume V_{gel} as a function of ε_{mm} and pH, revealing a closed-loop phase diagram with a central discontinuous transition. Color map indicates the degree of ionization α and solid lines mark constant pH values at pH − pK_a = 1 (blue), 3 (black), and 5 (red). (d, e) Density plots of V_{gel} and α showing sharp transitions at intermediate pH. Dashed black lines denote the discontinuous transition and triangles mark fluctuation peaks (see Figure 2). (f) Free energy barrier along the transition line from (d, e), where ΔpH = pH − pK_a. Parameters: width $N_x = N_y = 2$ and length $N_z = 6$ unit cells of size $N_p = 10$, containing a total of 1395 ionizable monomers.

and immersed in an aqueous solution (Figure 1a,b). Each bead represents a monomer of diameter b = 0.72, nm, with short-range van der Waals and solvent interactions modeled via a bead−bead attraction of strength ε_{mm}. Charge−structure coupling is modeled by allowing each monomer to undergo acid dissociation reaction, $A^0 \rightleftharpoons A^- + H^+$, where the ionization probability α_i of a monomer i at position $\mathbf{r}_i$ is[18,42]

$$\frac{\alpha_i}{1-\alpha_i} = 10^{\mathrm{pH}-\mathrm{p}K_a} e^{-\beta\psi(\mathbf{r}_i)e_0} \tag{1}$$

with pK_a the dissociation constant, $\psi(\mathbf{r}_i)$ the local electrostatic potential which depends on the global structure of the gel, and e_0 the elementary charge. All charged species, including monovalent salt ions at concentration $c_s = 10^{-3}$ M, are explicitly modeled (see Figure 1a,b). $\psi(\mathbf{r}_i)$ is obtained by fully solving the electrostatic Poisson equation via Ewald summation, thus eq 1 explicitly takes into account long-range electrostatic correlations and provides more accurate predictions compared to mean-field approximations[43] that were commonly employed in previous studies.[17,23] Hydrodynamic effects are included using the DPD solvent method[44] (see Methods section for details).

■ RESULTS AND DISCUSSION

Equilibrium pH−Temperature Phase Diagram

To understand the actuation behavior, we first calculate the equilibrium phase diagram of a nanogel particle immersed in an aquaous solution. We initially focus on an elongated nanogel which is a prototypical system for hydrogel-based soft actuators and artificial muscles.[45] Based on experimental observations[21,46] and theoretical predictions,[22] we anticipate that a hydrogel containing ionizable groups exhibits a critical point beyond which the collapse−swelling transition is discontinuous.

We measure the response of gel volume V_{gel} and average ionization α to changes in pH and monomer−monomer attraction ε_{mm}/k_BT. V_{gel} is obtained from the convex hull of the gel monomers and pH denotes the pH of the surrounding solution (i.e., the reservoir). Interestingly, we find a sharp collapse−swelling transition only at intermediate pH values (Figure 1c−e), which suggests a closed-loop phase diagram bounded by two critical points. The discontinuous transition arises due to charge regulation coupling between the gel conformation and ionization [eq 1], leading to coexistence between an expanded charged gel and a collapsed uncharged gel. However, this charge regulation effect disappears in the limits of high and low pH for which the charge on the gel is constant ($\alpha \to 1$ or $\alpha \to 0$), see Figure 1d,e. Free-energy calculations (Figure 1f and Figure S1) show that the expanded and collapsed states are separated by a free-energy barrier at intermediate pH, confirming a discontinuous conformational transition. Note that the phase diagrams in Figure 1 depend only on the difference pH − pK_a and are valid for any pH values that are not too extreme: $-\log_{10}(c_s) < \mathrm{pH} < 14 + \log_{10}(c_s)$, so that the contribution from H$^+$ and OH$^-$ do not significantly affect the ionic strength. In our case, the salt concentration $c_s = 10^{-3}$ M and so the phase diagrams are valid for $3 < \mathrm{pH} < 11$.

Fluctuation analysis of V_{gel} and α (Figure 2) further shows two distinct peaks that indicate tentative locations of the two critical points (marked by triangles in Figure 1d,e). The peak locations are consistent for fluctuations in gel volume V_{gel} and ionization α, indicating that these are signatures of the two critical points. Finite-size scaling shows that the free-energy barrier increases with increasing gel volume (Figure S2 in

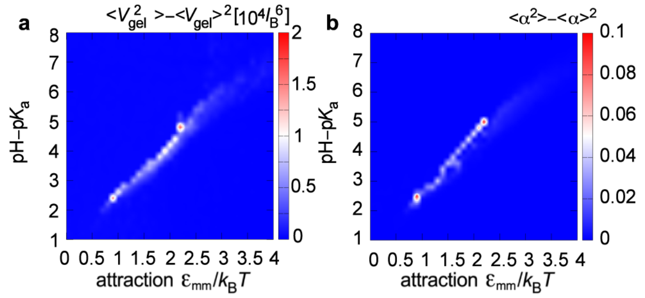

Figure 2. Equilibrium fluctuations in a polyelectrolyte nanogel. Relative fluctuations in (a) gel volume V_{gel} and (b) ionization degree α. Both quantities exhibit two distinct peaks, consistent with a discontinuous region bounded by two critical points located at $\mathrm{pH}^* - \mathrm{p}K_a = 2.5$, $\varepsilon^*_{\mathrm{mm}}/k_BT = 0.9$ and $\mathrm{pH}^* - \mathrm{p}K_a = 5$, $\varepsilon^*_{\mathrm{mm}}/k_BT = 2.2$.

Supporting Information), which further supports that the conformational change is a discontinuous transition at intermediate pH values. On the other hand, the barrier disappears at both high and low pH values indicating that a continuous transition occurs for both neutral (low pH, $\alpha \sim 0$) and fully ionized (high pH, $\alpha \sim 1$) nanogel (Figure 1f and Figure S3).

The location of the transition is not significantly affected by varying the shape of the gel or the cross-link distance (Figure S4), which implies that the phase diagram in Figure 1d,e is robust and is expected to apply to randomly cross-linked PE hydrogels. The existence of a discontinuous transition in gels due to charge is well-known,[21,22,46,47] but in these cases the discontinuous region was not bounded, presumably due to a limited range of parameters explored or the specific chemistry of the system. A closed-loop phase diagram was previously reported only for a polyampholyte gel.[17,46] Here we show that by exploring a full range of $\varepsilon_{\mathrm{mm}}/k_BT$ and pH values, a closed-loop phase diagram arises in a purely anionic hydrogel. In fact, this phase diagram may explain why the experimentally observed hydrogel volume transition is sharpest at intermediate temperature and pH.[48−50] A closed loop topology is also consistent with previous investigations that show continuous collapse—swelling for both neutral[51] and fully charged[25,52] gels in an aqueous solution.

The discontinuous transition at intermediate pH is consistent with the behavior of linear polyelectrolytes, where a pH-driven, discontinuous first-order transition was initially predicted by theory[53] and later confirmed in simulations.[18,54] The common underlying mechanism in both hydrogels and weak polyelectrolytes is a strong, nonlinear coupling between the ionization state and the polymer conformation. Similar phenomena have also been observed in weak hydrophobic hydrogels under pressure.[55] For a gel under external stress, the CR effect gives rise to strong mechano−electrostatic coupling, mediated through the dependence of α and ψ, eq 1. This will be investigated below when discussing actuation performance.

Whether the full closed-loop phase diagram is experimentally realizable depends on the range of effective $\varepsilon_{\mathrm{mm}}/k_BT$ values that can be probed in a specific system. The short-range interaction $\varepsilon_{\mathrm{mm}}$ incorporates all nonelectrostatic interactions, such as hydrophobic, van der Waals, and hydrogen bonding. Therefore, $\varepsilon_{\mathrm{mm}}$ can either increase or decrease with temperature, depending on the chemistry of a specific system. If the main contribution to $\varepsilon_{\mathrm{mm}}$ is van der Waals or intra-PE hydrogen bonding, we expect $\varepsilon_{\mathrm{mm}}/k_BT$ to decrease with increasing temperature and the critical point at $\varepsilon_{\mathrm{mm}}/k_BT \approx 1$ represents the upper critical solution temperature (UCST), while the second critical point at $\varepsilon_{\mathrm{mm}}/k_BT \approx 2.2$ represents the lower critical solution temperature (LCST), see ref 56 for a recent example. On the other hand, if the origin of $\varepsilon_{\mathrm{mm}}$ is hydrophobic, then $\varepsilon_{\mathrm{mm}}/k_BT$ could increase with temperature and the critical point at $\varepsilon_{\mathrm{mm}}/k_BT \approx 1$ would represent LCTS.[46] If multiple types of chemical interactions are of comparable strength, $\varepsilon_{\mathrm{mm}}/k_BT$ could even be nonmonotonic with temperature, potentially yielding a complicated pH−temperature phase diagram. Regardless of these system specifics, the phase diagrams in Figure 1 are expected to generally describe a pH-sensitive hydrogel. We note that $\varepsilon_{\mathrm{mm}}$ can be mapped to the Flory χ parameter of a neutral polymer by mapping the critical point of the truncated-shifted LJ fluid, $T^*_{\mathrm{LJ}} \approx 1.1\varepsilon_{\mathrm{mm}}$, to the Flory−Huggins model, $\chi = 2T^*_{\mathrm{LJ}}/T \approx 2.2\varepsilon_{\mathrm{mm}}/k_BT$.[44]

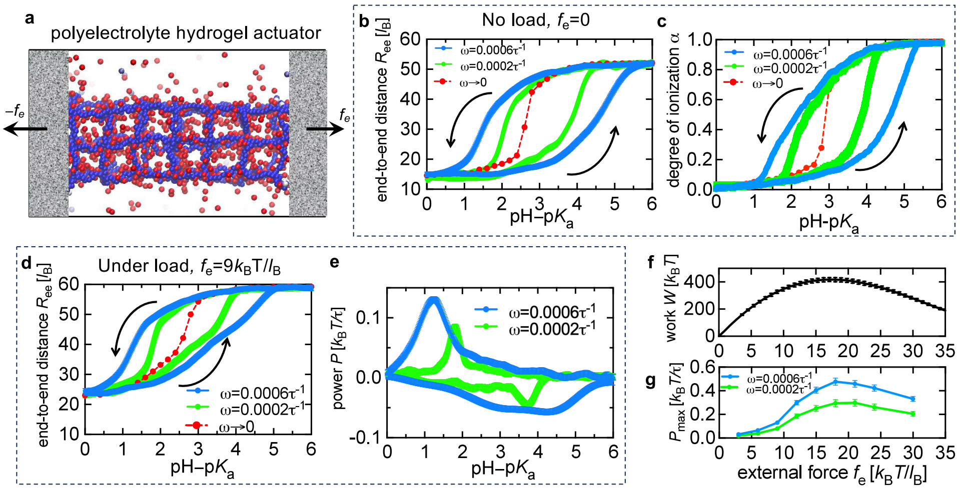

Figure 3. Polyelectrolyte hydrogel as a pH-responsive soft actuator. (a) An external force f_e is applied to the ends of the nanogel. (b, c) The response of a weak polyelectrolyte gel ($\mathrm{p}K_a = 4$) to pH ramping at no external load $f_e = 0$. (d, e) The response under load $f_e = 9k_BT/l_B$ (stress of about 2.5×10^5 Pa) with the power output, $P = -f_e dR_{\mathrm{ee}}/dt$. (f, g) The equilibrium work performed upon gel contraction and the maximum power $P_{\max}$ as a function of external force, note $\tau = 0.029$ ns. The error bars show standard errors (see Figure S12 for response variance). The arrows in (b)−(d) show the actuation direction in the hysteresis loop.

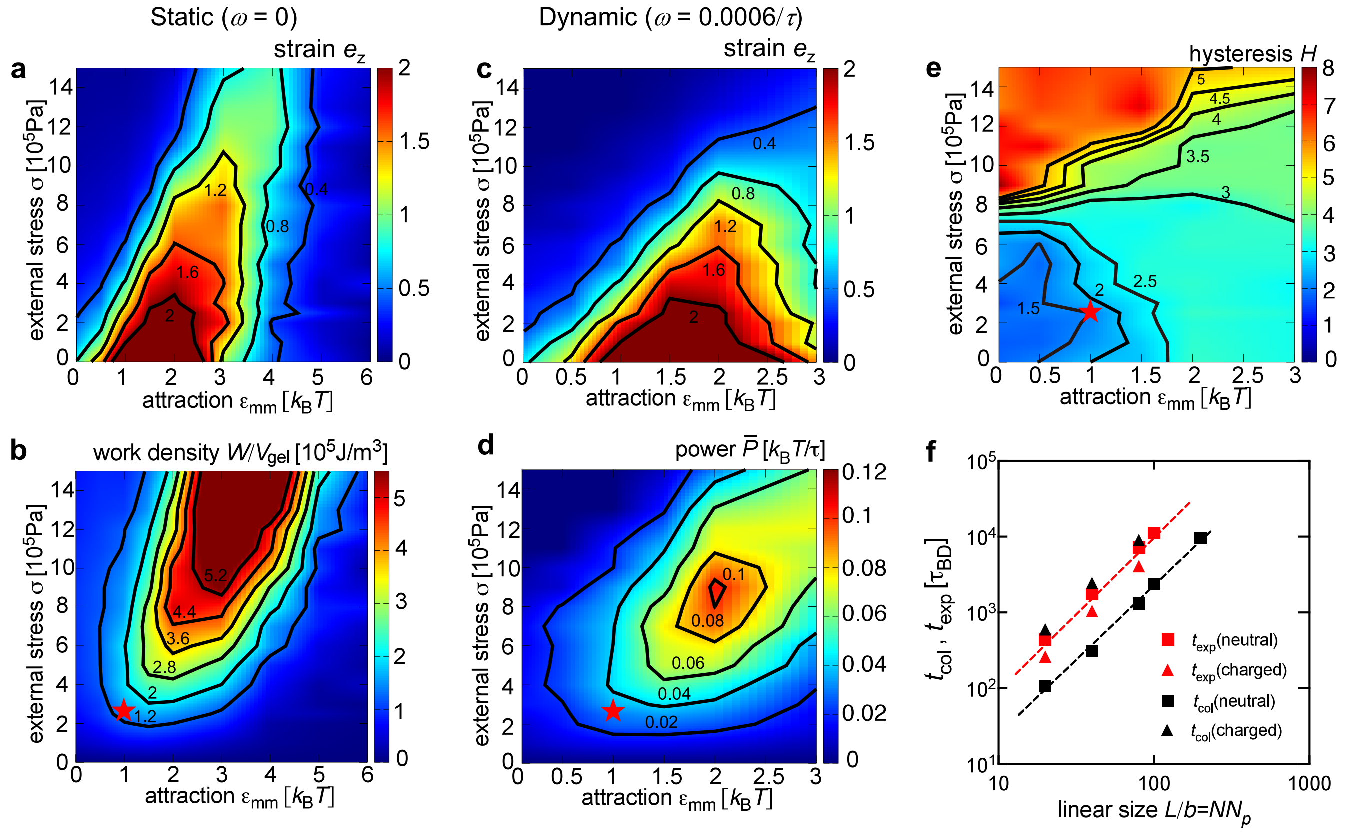

Figure 4. Performance of a hydrogel actuator: actuation strain, work density, power, hysteresis and response time scale. (a, b) Equilibrium strain and work density as a function of engineering stress σ and attraction ε_{mm}. (c−e) Strain e_z, mean power $\bar{P}$ [eq 2], and hysteresis (H) [eq 3] at ramping rate $\omega = 0.0006/\tau$. The red-colored star in (b), (d), and (e) marks the parameter point used in Figure 3b−e at which the nanogel demonstrates reasonable trade-off between high power density and low hysteresis. (f) Time scales for collapse t_{col} and expansion t_{exp} of a neutral gel (squares) and a fully charged gel (triangles) as a function of size L/b. The dashed lines indicate a slope of 2. The time is scaled in terms of the Brownian time for a free particle $\tau_{BD} = \tau/1.5 \approx 0.02$ ns.

Nonequilibrium Actuation Dynamics of pH-Responsive Nanogels

Having calculated the equilibrium phase diagram, we turn to kinetics and design a pH-responsive actuator. We introduce a constant force with magnitude f_e to the two ends of the nanogel (Figure 3a) and apply a zigzag time-varying pH cycle between $pH_0 = pK_a$ and $pH_1 = pK_a + 6$ with ramp rate $\omega = d(pH)/dt$ (see Methods). The total time to complete a full cycle is $t_f = 2(pH_1 - pH_0)/\omega$. Guided by the phase diagram (Figure 1d,e) we chose $\varepsilon_{mm} = k_BT$, which is close to the peak in equilibrium fluctuations (Figure 2) and is thus expected to result in a sharp and fast response. Hydrodynamics is resolved using the dissipative particle dynamics solvent (DPDS) method[44] that models an aqueous solution with time unit τ = 0.029 ns, while the ionization kinetics is modeled using the charge regulation-Monte Carlo (CR-MC) method[18] with realistic ionization rates $k_d \approx 10^7$ s^{-1}.[57−59]

We find that the end-to-end distance R_{ee} of the gel follows the pH cycle and shows hysteresis that becomes more pronounced at faster cycling rates (Figure 3b,d). The response under external load remains qualitatively the same compared to the zero-load case, but the conformations are more elongated due to the stretching by the external force. In all cases, the expansion is driven by the ionization of monomers and counterion osmotic pressure (Figure 3c; also see Movies S1 and S2 for visualizations of the conformational transition). Different cross-linking architectures, such as constant versus random cross-linking distance, and square versus diamond lattice do not affect the results (Figures S6 and S7). Thereby, our predictions are not sensitive to specific cross-linking details.

The maximum instantaneous power of the nanogel is $P_{max} \approx 0.1 k_BT/\tau$ obtained at the high-frequency limit ($\omega = 0.0006\tau^{-1}$) allowed by protonation kinetics[59] (Figure 3e). The corresponding power density is $P^{max}/V_{gel} \approx 10^6$ W/cm^3, which is about 6 orders of magnitude larger than that of skeletal muscles. For the gel to complete the transition through the characteristic pH interval $\Delta pH \approx 3$ (from $pH - pK_a$ = 1−4), the required response time scale can be estimated as $\tau_r = \Delta pH/\omega \approx 3/\omega$. The response time of the gel at a lower rate $\omega = 0.0002\tau^{-1}$ is $\tau_r \approx 0.4$ μs, using the DPD time scale τ = 0.029 ns,[44] which is at least 4 orders of magnitude faster than typical values for mammalian skeletal muscles[60,61] or macroscopic soft actuators.[62,63] The fast response and high power density are a consequence of the nanoscale width of the gel which permits fast transport of solvent. Moreover, a comparison with Langevin dynamics, which assumes a static solvent, shows that hydrodynamic interactions reduce the response time (Figure S8), demonstrating that solvent flow improves the responsiveness of nanogel actuators.

The work W performed during the contraction of the gel is $W = f_e \Delta R_{ee}$, with the change in the end-to-end distance $\Delta R_{ee} = R_{ee}(pH_1) - R_{ee}(pH_0)$. W reaches a maximum at force $f_e^* \approx 18 k_BT/l_B$ and decreases at larger forces that prevent

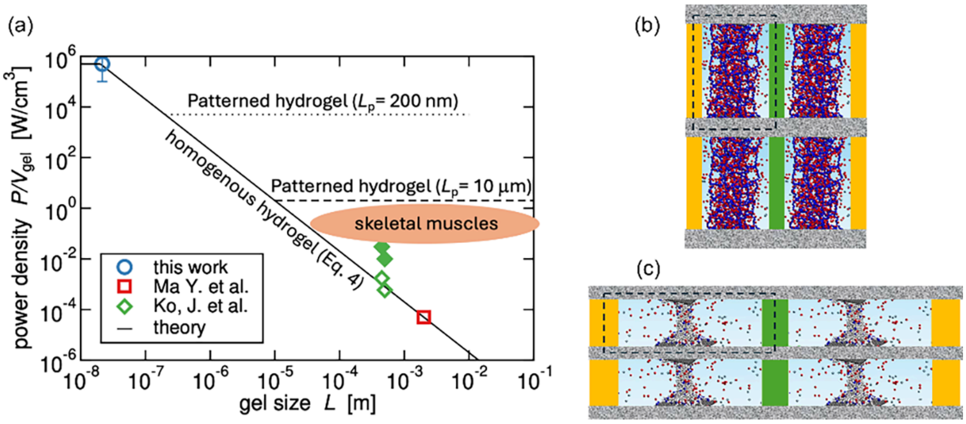

Figure 5. Power density of the hydrogel actuator and schematic design of a patterned gel. (a) Power density of the actuator. The solid black line is given by eq 4 with prefactor $C = 2 \times 10^{-4}$ W/m. Symbols show the simulation value for a simulated nanogel (circle) and literature values for a 2 mm hydrogel (square),[63] and a 450−500 μm hydrogel (solid diamonds, raw data)[66,67] with rescaling for the driving voltage to match our conditions (empty diamonds). The dashed and dotted lines are the predicted performance for a structured gel with pattern size L_p = 10 μm and L_p = 200 nm, respectively. (b, c) Design of the patterned actuator device formed by stacking individual nanogels into an array showing the expanded (b) and collapsed (c) state. Upon actuation, solvent flow occurs only locally within the unit cell (dashed lines). Orange and green bars denote flexible electrodes that are a source and sink of H^+ ions.

the gel from fully collapsing (Figure 3f). The optimal load translates to engineering stress $\sigma = f_e/A \approx 5 \times 10^5$ Pa, with the maximal cross-section area, $A = N_p^2 N_x N_y b^2 = 400b^2$, under which conditions the gel can elongate 2-fold. Moreover, the maximum work W^* at the force f_e^* is $W^* \approx 400k_BT$, corresponding to a work density of $W^*/V_{gel} \approx 150$ kJ/m^3. Thus, the maximum strain of the pH-driven gel actuator is comparable to that of skeletal muscles, while the stress and work density are an order of magnitude larger.[61] The maximum instantaneous power P_{max} at the high frequency limit ($\omega = 0.0006\tau^{-1}$) also exhibits a peak close to f_e^* (Figure 3g), suggesting that the nanogel actuator can yield favorable performance in terms of both work and power even at fast cycling rates.

Optimal Design Strategies: Work, Power and Hysteresis Effects

To explore the optimal design of the nanogel actuator, we calculate the end-to-end distance, work, power, and hysteresis over a full spectrum of working conditions (Figure 4). The equilibrium strain $e_z = \Delta R_{ee}/R_{ee}(\mathrm{pH}_0)$ and work density, $W(\omega \to 0)/V_{gel} = \sigma \Delta R_{ee}(\omega \to 0)/R_{max}$ are largest in the discontinuous region of the phase diagram (Figure 4a,b). The exact definition of the work density depends on whether we normalize by the volume of the collapsed or the expanded configuration. We use the later which provides a lower bound for the work density with $R_{max} = N_z N_p b$ being the fully extended end-to-end distance. At fast cycling rates the response is limited by the viscous drag (Figure 4c), consequently, the mean power per contraction,

$$\overline{P}(\omega) = W(\omega)\frac{\omega}{\mathrm{pH}_1 - \mathrm{pH}_0} \tag{2}$$

is maximal at intermediate stress σ and interaction strength ε_{mm} (Figure 4d). This observation underscores the crucial role of hydrodynamic effects: the slow relaxation dynamics at $\varepsilon_{mm}/k_BT > 2$ fail to keep pace with the pH ramping rate (also compare Figure 4a,c and Figure S9). The power density was obtained at the high-frequency limit allowable by protonation kinetics, $\omega = 0.0006/\tau$,[59] thus the work and power plots in Figure 4b,d effectively show the low and high-frequency limits of the actuator performance. A stronger monomer−monomer attraction leads to a larger stall force (Figure 4a), which represents the critical load above which the conformational transition is suppressed. This trend arises because a higher attraction strength stabilizes the collapsed gel.

To quantify the hysteresis $H(\omega)$ of the hydrogel response we calculate the effective width between the forward and reverse process,

$$H(\omega) = \frac{1}{\Delta R_{ee}(\omega)} \oint R_{ee}\, \mathrm{d(pH)} \tag{3}$$

as the integration area of the closed loop on the R_{ee}−pH plot divided by the total change in size $\Delta R_{ee}(\omega)$ (Figure 4e). Hysteresis is lowest at $\varepsilon_{mm}/k_BT \leq 1$, which coincides with the continuous region of the phase diagram (Figure 1d). These findings indicate that the overall optimal condition for actuator performance is close to a critical point, specifically the weak-interaction critical point at $\varepsilon_{mm}/k_BT \approx 1$, resulting in fast size changes with appreciable power output, but without strong hysteresis effects. The corresponding raw data is provided in Supplementary Figure S10.

The hysteresis arises from the free energy barrier (Figure 1f) as well as the viscous drag. In the discontinuous region ($\varepsilon_{mm}/k_BT \approx 1.5$) the barrier is high and we find a large hysteresis, whereas in the continuous region ($\varepsilon_{mm}/k_BT < 0.9$) the barrier disappears leading to low hysteresis (Figure 4e). At very strong interaction ($\varepsilon_{mm}/k_BT > 2$) the polymer−polymer friction also contributes to drag leading to enhanced hysteresis. A very similar pH-response hysteresis has recently been reported in an experimental system of weak polyelectrolyte brushes[64] and we expect the underlying mechanism that causes the hysteresis (solvent drag and free-energy barrier) are the same in both systems. Furthermore, to alleviate the reswelling hysteresis, preserving residual solvent in the collapsed nanogel may be helpful to avoid staling.[65] A practical strategy for promoting such solvent retention could involve moderately increasing the lower bound pH_0 of the operational pH window.

Collapse/Expansion Time Scales and Power Density

As the time scales of collapse, t_{col}, and expansion, t_{exp}, directly determine the maximum power, it is also essential to understand the impact of gel size L on the swelling−collapse dynamics. We consider a cubic nanogel where $N_x = N_y = N_z = N$ at cross-linking distance $N_{\mathrm{p}} = 10$ and calculate the expansion/collapse time scales as a function of the linear size $L/b = NN_{\mathrm{p}}$ for both fully charged and neutral gels (see Methods section for detailed protocols of collapse/expansion dynamics). Interestingly, we find that both the collapse and expansion time scales exhibit scaling with the gel size L as $t_{\mathrm{col}} \sim L^2$ and $t_{\mathrm{exp}} \sim L^2$ (Figure 4f) for both charged and neutral gels; also see Figure S11 for details on the determination of time scales. This scaling agrees with a theoretical prediction[35] and experimental measurements[37,40] for a swelling time scale of a neutral gel. Here we found that the same L^2 scaling also applies to fully charged gels. The expansion of a neutral gel is slower than its collapse (Figure 4f) in agreement with experimental data.[37] Moreover, based on Figure 4f, we infer that for a neutral nanogel of diameter 200 nm, the collapse time scale is $t_{\mathrm{col}} \approx 10^{-6}$ s, while for microgels with a diameter of 2 and 600 μm, the predicted expansion times are, respectively, $t_{\mathrm{exp}} \approx 2 \times 10^{-4}$ s and $t_{\mathrm{exp}} \approx 5$ s. These values are in the range of recent experimental time scales.[37,40,66]

Since the work per cycle is $W = f_{\mathrm{e}}\Delta R_{\mathrm{ee}}$ with the stress $\sigma \approx f_{\mathrm{e}}/L^2$ and the change in length ΔR_{ee} is proportional to L, it follows that the work density, $W/V_{\mathrm{gel}} \sim \sigma$, is a constant. Because the temporal response scales as L^2, the power density of the actuator scales as $P/V_{\mathrm{gel}} \sim L^{-2} \sim V_{\mathrm{gel}}^{-2/3}$. For the simulated nanogel actuator (Figures 3f and 4d), the mean power is about $0.04k_{\mathrm{B}}T/\tau \approx 0.5 \times 10^{-11}$ W and the gel volume is $V_{\mathrm{gel}} \approx N_xN_yN_zN_{\mathrm{p}}^3b^3 \approx 10^{-5}\ \mu\mathrm{m}^3$, thus the power density is $P_{\max}/V_{\mathrm{gel}} \approx 0.5 \times 10^{-6}\ W/\mu\mathrm{m}^3$. Using this data and the scaling we can predict the power density for an arbitrary gel size,

$$\frac{P}{V_{\mathrm{gel}}} = CL^{-2} \tag{4}$$

with the prefactor value $C \approx 2 \times 10^{-4}$ W/m obtained from simulation data, see Figure 5.

Comparing the prediction, eq 4, to recent experimental data on the maximal achieved hydrogel power density,[63,66,67] we find excellent aggrement (Figure 5). The raw data of refs 66 and 67 is obtained at a higher driving voltage of $\Delta\psi = 6V$, whereas in our simulations the change in pH is $\mathrm{pH}_1 - \mathrm{pH}_0 = 6$ (Figure 3), which corresponds to the change in electrochemical potential of $\Delta\psi = k_{\mathrm{B}}T(\mathrm{pH}_1 - \mathrm{pH}_0)\ln(10)/e_0 = 350$ mV. Rescaling by the ratio of driving voltages we find perfect agreement between experimental data and theoretical prediction (empty diamonds in Figure 5). The model is consistent with both simulations and the available experimental data, and thus appears to be able to predict the power density over a range of at least 10 orders of magnitude.

To determine how the power density depends on the physical and chemical properties of the gel, we calculate the response time scale by extending the theory of Tanaka[35] to gels under external stress. The power density can be estimated theoretically by considering that the gel exhibits maximum (equilibrium) stress $\sigma^{\max}$, which depends on the chemical details and electrochemical driving. Upon actuation, this stress is balanced by the external (working) stress σ, the viscous drag of the solvent σ_{drag} and inertia σ_{m} due to the mass of the actuator: $\sigma^{\max} = \sigma + \sigma_{\mathrm{drag}} + \sigma_{\mathrm{m}}$. To estimate the drag force we consider Stokes drag on each cross-link, $f_\zeta = 3\pi\eta\zeta v$, obtained by considering a flexible cross-link with $R_{\mathrm{g}} \sim \zeta$ and a Zimm model. The same result is obtained by considering a straight cross-link with force exerted on each monomer of the cross-link $f_1 = 3\pi\eta bv$ and multiplying by the number of monomers per cross-link, $f_\zeta = f_1\zeta/b$. The total stress due to drag is thus $\sigma_{\mathrm{drag}} \approx f_\zeta L/\zeta^3 \approx 3\pi\eta Lv/\zeta^2$. This underestimates the number of cross-links per ζ^3 by about a factor 2, while it overestimates drag per cross-link by about a factor 2 because, due to global solvent flow, not every cross-link experiences solvent speed v. Thus, the two approximations partially cancel out, yielding a reasonably accurate estimate of the drag. The actuation speed v determines the time scale for collapse/expansion $t_{\mathrm{col}} = Le_z/v \approx 3\pi\eta L^2e_z/(\sigma_{\mathrm{drag}}\zeta^2)$, with $e_z = \Delta R_{\mathrm{ee}}/L$ the actuation strain. The inertial term can be estimated as $\sigma_{\mathrm{m}} \sim Le_z\rho/t_{\mathrm{col}}^2$, with ρ the mass density. Since the response time is $t_{\mathrm{col}} > 1$ ns, even for the smallest possible nanogels (Figure 4f), inertia is always negligible compared to viscous drag, and we can approximate $\sigma_{\mathrm{drag}} \approx \sigma^{\max} - \sigma$. The power density can therefore be estimated as

$$\frac{P}{V_{\mathrm{gel}}} = \frac{\sigma e_z}{t_{\mathrm{col}}} \approx \frac{\zeta^2\sigma(\sigma^{\max} - \sigma)}{3\pi\eta}L^{-2} \tag{5}$$

This equation reveals that the physical origin of the L^{-2} scaling we found in simulations [eq 4] is solvent drag, with the prefactor $C^{\mathrm{theory}} = \zeta^2\sigma(\sigma^{\max} - \sigma)/(3\pi\eta)$. The maximum value of power density occurs at $\sigma = \sigma^{\max}/2$. For the simulated actuator we found $\sigma^{\max} = 5 \times 10^5$ Pa (Figure 3) and using the water viscosity $\eta = 10^{-3}$ Pa s and $\zeta \sim 5$ nm yields a prediction $C^{\mathrm{theory}} = 1.7 \times 10^{-4}$ W/m, which is remarkably close to the value obtained directly from simulations, $C \approx 2 \times 10^{-4}$ W/m, see Figure 5.

Equation 5 shows that increasing the maximum power density can be achieved by reducing the solvent viscosity η or increasing the product $\sigma^{\max}\zeta^2$. Since the maximum strain and cross-link distance are not independent (we can argue that $\sigma^{\max} \propto \zeta^{-3}$), the product $\sigma^{\max}\zeta^2$ could be increased by decreasing ζ or by increasing the driving voltage or pH range. However, these parameters cannot be optimized arbitrarily due to physical constraints and in fact are already chosen to be close to optimal. Therefore, the main route to substantially increase the power density is by reducing the size L.

Both theory and experimental data show that large gels suffer from low power density (Figure 5a). To overcome this deficiency of bulk gels, we propose that a high power density in a bulk gel can be obtained by using a structured gel, stacking strips of a hydrogel together with a proton source (e.g., flexible electrodes; see Figure 5b for a schematic demonstration). Such a patterned structure does not require bulk solvent flow, but only local flow within each unit cell and therefore the response time and power density are determined by the pattern size L_{p} and not the bulk size of the gel. For example, to attain a power density similar to that of skeletal muscle requires a pattern width $L_{\mathrm{p}} \approx 30\ \mu$m (Figure 5). This width indeed corresponds to the width of individual muscle fibers, suggesting that solvent drag and chemical diffusion are the fundamental limiting factors on power output in both synthetic and biological systems.

Effects of Ion Diffusion and Protonation Kinetics

The time scale for ion diffusion across the hydrogel is $t_{\mathrm{diff}} = L^2/(2D)$, which, for typical ion diffusivity $D \approx \mathrm{nm}^2/\mathrm{ns}$, is faster than the fastest ramping rates considered in Figure 3 and Figure 4 ($L_x/b = N_x N_p = 20$). Note that H^+ ions diffuse even faster, $D \approx 10\ \mathrm{nm}^2/\mathrm{ns}$, due to Grotthuss mechanism. Since the time scales of collapse/expansion (Figure 4f) and ion diffusion show the same scaling ($\sim L^2$), we predict that ion diffusion across the gel is not expected to be a limiting process, even for bulk gels, which is consistent with previous studies.[68] However, depending on the gel chemistry, it is possible that ion diffusivity in the gel would be very slow. In this case, the collapse time scale in eq 5 would be limited by the diffusion time, $t_{\mathrm{col}} \approx t_{\mathrm{diff}} = L^2/(2D)$ and consequently the prefactor C in eq 4 that determines the power density would be limited by $C \leq 2D\sigma e_z$. Thus, the effect of slow ion diffusion would reduce the prefactor C but would not change the scaling with gel size.

The gel actuator is driven by protons and requires a proton source snd sink, e.g., an electrode, and ions are supplied by an electrolyte reservoir. Thus, ion/proton transport from the source to the gel, which is not taken into account by our simulation setup, could be another limiting factor on the kinetics and could be important especially at low ion concentration. To minimize the transport time scale and achieve fast response time, the proton/source sink should be placed next to the gel, and it could itself be a soft electrode, e.g., a conducting polymer (Figure 5b,c).

The power scaling prediction [eq 4] is limited at low L by the ionization or protonation kinetics, $P/V_{\mathrm{gel}} \leq \sigma e_z k_d$ (see Figure 5). The protonation dynamics is governed by typical weak acid dissociation rate $k_d \approx 10^5\ \mathrm{s}^{-1} - 10^7\ \mathrm{s}^{-1}$ and association rate $k_a \approx 10^{11-\mathrm{pH}}\ \mathrm{s}^{-1}$,[57−59] which do not depend on the gel size. For example, the actuation power in Figure 4d is obtained at the high-frequency limit allowable by proton dissociation dynamics. Since the response time due to solvent drag scales as L^2, we conclude that the protonation dynamics can be a limiting factor only for nanoscale gels ($L \lesssim 200$ nm) or extremely weak PEs where, for a weak acid gel, the collapse occurs at high pH. Thus, our predictions for power output of gels larger than 200 nm are not affected by changing k_d and k_a within experimental range.

■ CONCLUSIONS

In this work we dynamically modeled the coupling between charge and structure in polyelectrolyte nanogels by explicitly simulating the protonation of individual dissociable groups. This approach allowed us to compute the pH−$\varepsilon_{\mathrm{mm}}/T$ and V_{gel}−$\varepsilon_{\mathrm{mm}}/T$ conformational diagrams, revealing a closed-loop phase diagram with a discontinuous swelling−collapse transition bounded by two critical points. By explicitly incorporating hydrodynamic interactions, we calculated the response dynamics and demonstrated that hydrogels can act as efficient pH-driven actuators. The maximum strain achieved is comparable to that of skeletal muscle, while the tensile stress and work density exceed it by an order of magnitude. Combining insight from simulation data, analytical theory, and comparison with experiments, we identify two key design principles for obtaining high actuation performance: (a) optimal actuation that combines high power density and low hysteresis occurs near a critical point on the pH−temperature phase diagram, and (b) the power density scales inversely with the square of the gel size, $P/V_{\mathrm{gel}} = CL^{-2}$, with the prefactor, $C \sim 10^{-4}$ W/m, that depends on chemical and structural details.

These results highlight a key limitation of bulk hydrogels: their response time is fundamentally constrained by solvent drag and ion diffusion. To overcome this, we propose a biomimetic architecture composed of nano or microscale hydrogel strips integrated with a local proton source (e.g., flexible electrodes). Similar to the fibrillar structure of biological muscles, the patterned arrangement ensures the solvent transport occurs only locally within each cell (Figure 5b,c), thereby circumventing the slow kinetics of bulk solvent flow. The power density of the patterned gel is not limited by the size of the material, but is instead determined by the cell width L_p. Such a structured material could achieve millisecond-scale actuation with high power output, which should be very useful for applications in soft robotics and artificial muscles. If a gradual, well-controlled response is required, a composite gel that incorporates polymers with distinct chemical properties may provide a promising strategy for engineering programmable response. More broadly, our study provides mechanistic insight into the nonequilibrium response of hydrogels, revealing the dynamic interplay among conformation, ionization, and solvent flow. The modeling framework that combines charge regulation with dissipative particle dynamics offers a platform for studying charge−structure−hydrodynamic coupling in a variety of macromolecular systems and soft materials.

■ METHODS

Model Details

We employ a standard coarse-grained model where ions and monomers are represented as spheres of diameter b, interacting via a shifted and truncated Lennard-Jones (LJ) potential,

$$U_{\mathrm{LJ}} = \begin{cases} 4\varepsilon\left[\left(\dfrac{b}{r_{ij}}\right)^{12} - \left(\dfrac{b}{r_{ij}}\right)^{6} + C\right] & r_{ij} \leq r_{\mathrm{cut}} \\ 0 & r_{ij} > r_{\mathrm{cut}} \end{cases} \tag{6}$$

where ε is the coupling constant and r_{ij} represents the distance between particles i and j. We use a cutoff $r_{\mathrm{cut}} = 3b$ and constant shift $C = 3^{-6} - 3^{-12}$ for intra-PE interactions, while all other LJ interaction are purely repulsive, corresponding to Weeks−Chandler−Andersen (WCA) potential with $r_{\mathrm{cut}} = 2^{1/6}b$ and $C = 1/4$. The coupling constant for ion−ion and ion−monomer interactions is set to $\varepsilon_{\mathrm{ii}} = \varepsilon_{\mathrm{im}} = k_B T$, whereas the monomer−monomer interaction $\varepsilon_{\mathrm{mm}}$ captures all short-range interactions (van der Waals, hydrophobic, and excluded volume) and can be mapped to the effective χ parameter of a neutral polymer $\chi \approx 2.2\varepsilon_{\mathrm{mm}}/k_B T$, which determines the solvent quality.[18] Neighboring monomers are bonded via a harmonic potential $U_{\mathrm{bond}}(r_{ij}) = K_{\mathrm{bond}}(r_{ij} - r_0)^2$ with spring constant $K_{\mathrm{bond}} = 200k_B T/b^2$ and bond length $r_0 = 2^{1/6}b$.

The system configurations are evolved employing the standard velocity-Verlet MD algorithm, while ionization states [eq 1] and ion exchange are sampled using an efficient charge regulation MC (CR-MC) solver[18] which is equivalent to the grand-reaction method.[69] We model all charged entities explicitly and perform grand-canonical MC exchange of dissociated ions (H^+) and monovalent salt cations (S^+) and anions (S^-) with a reservoir at a given pH and monovalent salt concentration $c_s = 10^{-3}$ M. The Bjerrum length, which sets the strength of electrostatic interactions, is $l_B = \beta e_0^2/(4\pi\varepsilon_{\mathrm{sol}})$, where $\beta = 1/(k_B T)$, k_B is Boltzmann constant, T is the absolute temperature, and $\varepsilon_{\mathrm{sol}}$ is the solvent permittivity, resulting in $l_B = b = 0.72$ nm for a hydrogel at room temperature. Electrostatic interactions are calculated using particle−particle particle−mesh (PPPM) algorithm[70] with relative force accuracy 10^{-3}.

To investigate the equilibrium phase diagram, we employ the standard Langevin dynamics simulations. The phase transition dynamics of PE are influenced by hydrodynamic interactions (HI).[71−74] Thus, for the study of nonequilibrium collapse/expansion dynamics of nanogels, we account for HI by combining the CR-MC solver with a method based on dissipative particle dynamics (DPD)[75] that couples the solute (gel) particles to the DPD solvent (DPDS).[44] Simulations were conducted using the LAMMPS package,[76] where the CR-MC method[18] and the DPDS method[44] are implemented.

Langevin Dynamics Simulations

For the investigations of equilibrium phase diagram, we employ the standard Langevin thermostat with damping time τ_d that is equal to the simulation time scale $\tau_d = b\sqrt{m/k_BT}$, with m the mass of the monomer. The integration time step of Langevin simulations is $\Delta t = 0.005\tau_d$. The simulation cell is a cubic box of size $L = 160b$ with applied periodic boundary conditions (PBC), we use $pK_a = 3$ and pH range from 4 to 11. We perform a chain of $n_{MC} = 50$ MC steps (reaction steps including ion insertion/deletion and acid dissociation/association) every $n_{every} = 500$ MD time steps in Langevin dynamics simulations. To equilibrate the system, we conduct simulated annealing for $2.5 \times 10^3\tau_d$ using a linear temperature ramp from starting temperature $T_s = 2T$ and ending with temperature T. The production runs of $3 \times 10^4\tau_d$ are carried out to sample the equilibrium properties at constant temperature T during which the configurations are sampled every $25\tau_d$. Free-energy calculations are performed using the metadynamics method[77,78] where we use a bin size $0.4b$ and a "Gaussian-hill" weight $0.01k_BT$ with hills deposited every 100 MD steps. To obtain sufficiently smooth free-energy profiles, we conduct longer production runs which last for $2.5 \times 10^5\tau_d$. For producing the equilibrium structure we use PPPM force accuracy of 10^{-3}, whereas for free energy calculations we utilize higher force accuracy of 10^{-5}. To demonstrate a sharp transition in phase diagrams (Figure 1) we utilize a fine grid near the transition line with lattice spacing 0.1 in pH and 0.05 in $\beta\varepsilon_{mm}$, whereas outside this region a coarser grid with 0.2 in pH and 0.1 in $\beta\varepsilon_{mm}$ is employed to reduce the total computational cost.

Dissipative Particle Dynamics Simulations

The incorporation of hydrodynamic interactions (HI) is essential for accurately modeling the nonequilibrium kinetics of the system. To study the actuation performance, we therefore employ a hydrodynamic solver based on dissipative particle dynamics (DPD).[75] Our method explicitly accounts for HI by coupling the ions and hydrogels to a DPD solvent (DPDS).[44] The method introduces explicit coarse-grained DPD solvent particles and ensures momentum conservation.

The monomers and ions are immersed in a DPD solvent characterized by parameters typical for an aqueous water solution: particle density $\rho = 3r_c^{-3}$, cutoff distance $r_c = \lambda = 0.646$ nm, friction parameter $\gamma = 4.5k_BT\tau/r_c^2$, with $\tau = \lambda\sqrt{m/(k_BT)}$ the standard molecular dynamics simulation time unit (also the time unit in DPD simulation), m the mass of the particles, and interaction prefactor $a_{ij} = 78k_BT$[44]). The coupling between the solute components (monomers and ions) and the DPD solvent is achieved by friction parameter $\gamma_s = 5\gamma$ and cutoff distance $r_s = r_c$. This setting yields the typical diffusion constant of ions and monomers $D \approx 0.078\lambda^2/\tau \approx 1$ nm^2/ns ($\tau \approx 0.029$ ns = 29 ps). Details on the DPD interaction potentials can be found in ref.[44] The system is evolved using the velocity-Verlet integrator with a time step of $\Delta t = 0.0125\tau$. The simulation box size is $L_x = L_y = 80b$, $l_z = 100b$ with PBC and we employ $pK_a = 4$ and pH range from 4 to 10. When plotting the collapse/expansion time scales in Figure 4f), we scale the time in terms of the Brownian time for a free particle $\tau_{BD} = b^2/(24D)$ (b = 0.72 nm; $\tau \approx 1.5\tau_{BD}$).

To model ionization kinetics we perform a chain of $n_{MC} = 300$ attempted MC reaction steps (including ion insertion/deletion and acid dissociation/association) every $n_{every} = 5000$ MD time steps in DPD simulations. The rate of acid dissociation moves in a gel with $N \approx 1400$ monomers is thus $k_d \sim \frac{1}{4}n_{MC}\Gamma/(n_{every}\Delta tN) \approx 2.7\Gamma\cdot 10^7$ s^{-1}, with Γ the MC acceptance ratio. Since $\Gamma \sim 0.5$, we get the dissociation rate that is at the upper limit of experimental values $k_d \approx 10^5$ s^{-1} ∼ 10^7 s^{-1}.[57−59] The acid association rate depends on the pH and is $k_a \approx 10^{11-\mathrm{pH}}$s^{-1},[59] however, we consider a gel that is a typical weak acid where the collapse occurs at pH ∼ 4 and we thus approximate $k_a \sim k_d$ (the number of attempted dissociation and association MC moves is the same). Since the gel conformational response is slower than ionization for gel size $L > 50$ nm, the local charge distribution is expected to be in quasi-equilibrium and thus changing ionization rates or Monte Carlo sampling details is not expected to significantly affect the gel response dynamics.

Protocol for pH Ramping and Inducing Collapse/Expansion

The pH-ramp simulations (Figure 3) are performed under a constant extensive force with magnitude f_e applied to the two ends of the hydrogel. The external force is applied to the terminal beads in the gel network along the primary axis of deformation. We have performed complementary simulations where the end points are grafted to the two walls and the loading force is applied to the two walls. We observed no statistically significant differences in the resulting actuation response between the two setups (Figure S5). Thus, the model details of the gel end tethering has a negligible effect on response dynamics. We use a zigzag time-varying pH cycle with ramp rate

$$\mathrm{pH}(t) = \begin{cases} \mathrm{pH}_0 + \omega t & 0 \le t \le t_f/2 \\ \mathrm{pH}_1 - \omega(t - t_f/2) & t_f/2 < t \le t_f \end{cases} \tag{7}$$

where ω is the ramping rate, $\mathrm{pH}_0 = 4$ is the initial pH value, $\mathrm{pH}_1 = 10$ the value at $t = t_f/2$, and the total time to complete a full cycle is $t_f = 2(\mathrm{pH}_1 - \mathrm{pH}_0)/\omega$.

In Figure 4d, we examine the impact of nanogel size on the collapse and expansion dynamics of both neutral ($\alpha = 0$) and charged ($\alpha = 1$) nanogels. In the study of gel collapse, we first equilibrate the gel in the expanded state using purely repulsive WCA short-range interaction between monomers, and the collapse is induced by introducing an attractive LJ interaction $\varepsilon_{mm} = 3k_BT$ (for $\alpha = 1$) or $\varepsilon_{mm} = k_BT$ (for $\alpha = 0$). Conversely, for investigating gel expansion we follow the reverse process; equilibrium structures are initially generated with $\varepsilon_{mm} = 3k_BT$ (for $\alpha = 1$) or $\varepsilon_{mm} = k_BT$ (for $\alpha = 0$), followed by a change to WCA interaction to initiate the expansion. We used a salt-free solution (only counterions for the charged gel) to investigate the two limits: neutral gel and full electrostatic repulsion. We anticipate that increasing the salt concentration would screen electrostatic interactions, but since both charged and neutral gels show the same scaling, we conclude that changing salt concentration would not affect the scaling.

Model Limitations

The coarse-grained model does not capture the effects of varying dielectric polarizability and the orientational ordering of water near ions,[79−81] which can enhance electrostatic coupling at small ion−ion distances. Ion and water diffusion are generally enhanced in polarizable compared to nonpolarizable models.[82] We also approximate the Bjerrum length as a constant independent of temperature, l_B = 0.72 nm, which is supported by the fact that the relative permittivity of water ε_{sol} decreases from $\varepsilon_{sol} \approx 82$ to $\varepsilon_{sol} \approx 65$ as the temperature increases from T = 10 °C to T = 60 °C,[83] resulting in l_B being only weakly affected across the typical temperatures of hydrogels.[50] For example, at 60 °C we underestimate the Bjerrum length l_B by a factor 1.07. Thus, our model employs a lower bound for electrostatic interaction strength. A more accurate description of water ordering, polarizability, and Bjerrum length dependence on temperature is anticipated to enhance the transport and the response of charge to conformational changes, potentially improving the actuator's performance. Furthermore, we did not consider ion-specific short-range interactions or multivalent ions, which may cause deviations from our prediction.[84,85] Establishing whether using multivalent ions can lead to even higher power density of the hydrogel presents a compelling direction for future research.

■ ASSOCIATED CONTENT

Supporting Information

The Supporting Information is available free of charge at https://pubs.acs.org/doi/10.1021/acs.macromol.5c03370.

Additional characterization of polyelectrolyte nanogels (PDF)

Movie S1 (MP4)

Movie S2 (MP4)

■ AUTHOR INFORMATION

Corresponding Author

Tine Curk – *Department of Materials Science and Engineering, Department of Physics and Astronomy, Johns Hopkins University, Baltimore, Maryland 21218, United States;* orcid.org/0000-0002-2167-5336; Email: tcurk@jhu.edu

Author

Jiaxing Yuan – *Advanced Materials Thrust, Function Hub, The Hong Kong University of Science and Technology (Guangzhou), Guangzhou 511453, China; Research Center for Advanced Science and Technology, University of Tokyo, Tokyo 153-8904, Japan;* orcid.org/0000-0001-9890-4961

Complete contact information is available at: https://pubs.acs.org/10.1021/acs.macromol.5c03370

Notes

The authors declare no competing financial interest.

■ ACKNOWLEDGMENTS

This work was supported by the National Science Foundation, CBET Division, Biosensors Program, Award Number 2402407. J.Y. acknowledges the startup funds provided by HKUST(GZ) and the National Natural Science Foundation of China (Grant No. 22503076). The simulations were partially performed using the Advanced Research Computing at Hopkins (rockfish.jhu.edu), which is supported by the National Science Foundation (NSF) grant number OAC 1920103. We thank Erik Luijten, Hajime Tanaka, James D. Farrell, Michael Falk, and Turash Haque Pial for discussions and comments on the manuscript.

■ REFERENCES

(1) Xia, L.-W.; Xie, R.; Ju, X.-J.; Wang, W.; Chen, Q.; Chu, L.-Y. Nano-structured smart hydrogels with rapid response and high elasticity. *Nature Comm.* **2013**, *4*, 2226.

(2) Karg, M.; Pich, A.; Hellweg, T.; Hoare, T.; Lyon, L. A.; Crassous, J. J.; Suzuki, D.; Gumerov, R. A.; Schneider, S.; Potemkin, I. I.; Richtering, W. Nanogels and microgels: From model colloids to applications, recent developments, and future trends. *Langmuir* **2019**, *35*, 6231−6255.

(3) Mann, B. A. F.; Kremer, K.; Lenz, O.; Holm, C. Hydrogels in poor solvents: A molecular dynamics study. *Macromol. Theory Simul.* **2011**, *20*, 721−734.

(4) van der Linden, H.; Westerweel, J. In *Encyclopedia of Microfluidics and Nanofluidics*; Li, D., Ed.; Springer US: Boston, MA, 2013; pp 1−5.

(5) Ge, S.; Li, J.; Geng, J.; Liu, S.; Xu, H.; Gu, Z. Adjustable dual temperature-sensitive hydrogel based on a self-assembly cross-linking strategy with highly stretchable and healable properties. *Mater. Horiz.* **2021**, *8*, 1189−1198.

(6) Mok, S.; Al Habyan, S.; Ledoux, C.; Lee, W.; MacDonald, K. N.; McCaffrey, L.; Moraes, C. Mapping cellular-scale internal mechanics in 3D tissues with thermally responsive hydrogel probes. *Nature Comm.* **2020**, *11*, 4757.

(7) Gupta, P.; Vermani, K.; Garg, S. Hydrogels: From controlled release to pH-responsive drug delivery. *Drug Discovery Today* **2002**, *7*, 569−579.

(8) Glazer, P. J.; van Erp, M.; Embrechts, A.; Lemay, S. G.; Mendes, E. Role of pH gradients in the actuation of electro-responsive polyelectrolyte gels. *Soft Matt.* **2012**, *8*, 4421−4426.

(9) Han, Z.; Wang, P.; Mao, G.; Yin, T.; Zhong, D.; Yiming, B.; Hu, X.; Jia, Z.; Nian, G.; Qu, S.; Yang, W. Dual pH-responsive hydrogel actuator for lipophilic drug delivery. *ACS Appl. Mater. Interfaces* **2020**, *12*, 12010−12017.

(10) Košovan, P.; Richter, T.; Holm, C. Modeling of polyelectrolyte gels in equilibrium with salt solutions. *Macromolecules* **2015**, *48*, 7698−7708.

(11) Shao, Z.; Wu, S.; Zhang, Q.; Xie, H.; Xiang, T.; Zhou, S. Salt-responsive polyampholyte-based hydrogel actuators with gradient porous structures. *Polym. Chem.* **2021**, *12*, 670−679.

(12) Schreyer, H. B.; Gebhart, N.; Kim, K. J.; Shahinpoor, M. Electrical activation of artificial muscles containing polyacrylonitrile gel fibers. *Biomacromol* **2000**, *1*, 642−647.

(13) Morales, D.; Palleau, E.; Dickey, M. D.; Velev, O. D. Electro-actuated hydrogel walkers with dual responsive legs. *Soft Matt* **2014**, *10*, 1337−1348.

(14) Li, C.; Lau, G. C.; Yuan, H.; Aggarwal, A.; Dominguez, V. L.; Liu, S.; Sai, H.; Palmer, L. C.; Sather, N. A.; Pearson, T. J.; Freedman, D. E.; Amiri, P. K.; de la Cruz, M. O.; Stupp, S. I. Fast and programmable locomotion of hydrogel-metal hybrids under light and magnetic fields. *Sci. Robot.* **2020**, *5*, na.

(15) Li, M.; Pal, A.; Aghakhani, A.; Pena-Francesch, A.; Sitti, M. Soft actuators for real-world applications. *Nature Reviews Materials* **2022**, *7*, 235−249.

(16) Sean, D.; Landsgesell, J.; Holm, C. Computer simulations of static and dynamical properties of weak polyelectrolyte nanogels in salty solutions. *Gels* **2018**, *4*, 2.

(17) Zheng, B.; Avni, Y.; Andelman, D.; Podgornik, R. Charge regulation of polyelectrolyte gels: Swelling transition. *Macromolecules* **2023**, *56*, 5217.

(18) Curk, T.; Yuan, J.; Luijten, E. Accelerated simulation method for charge regulation effects. *J. Chem. Phys.* **2022**, *156*, 044122.

(19) Brito, M. E.; Höpner, E.; Beyer, D.; Holm, C. Modeling swelling of pH-responsive microgels: Theory and simulations. *Macromolecules* **2025**, *58*, 2494−2507.

(20) López-Flores, L.; Olvera de la Cruz, M. Charge regulation effects on colloidal mixture nanoparticles. *J. Chem. Phys.* **2025**, *163*, na.

(21) Tanaka, T.; Fillmore, D.; Sun, S.-T.; Nishio, I.; Swislow, G.; Shah, A. Phase transitions in ionic gels. *Phys. Rev. Lett.* **1980**, *45*, 1636−1639.

(22) Polotsky, A. A.; Plamper, F. A.; Borisov, O. V. Collapse-to-swelling transitions in pH- and thermoresponsive microgels in aqueous dispersions: The thermodynamic theory. *Macromolecules* **2013**, *46*, 8702−8709.

(23) Longo, G. S.; Olvera de la Cruz, M.; Szleifer, I. Molecular theory of weak polyelectrolyte gels: The role of pH and salt concentration. *Macromolecules* **2011**, *44*, 147−158.

(24) Li, H.; Ng, T. Y.; Yew, Y. K.; Lam, K. Y. Modeling and simulation of the swelling behavior of pH-stimulus-responsive hydrogels. *Biomacromolecules* **2005**, *6*, 109−120.

(25) Yin, D.-W.; Yan, Q.; de Pablo, J. J. Molecular dynamics simulation of discontinuous volume phase transitions in highly-charged crosslinked polyelectrolyte networks with explicit counterions in good solvent. *J. Chem. Phys.* **2005**, *123*, 174909.

(26) Erbas, A.; Olvera de la Cruz, M. Energy conversion in polyelectrolyte hydrogels. *ACS Macro Lett.* **2015**, *4*, 857−861.

(27) Li, H.; Erbas, A.; Zwanikken, J.; Olvera de la Cruz, M. Ionic conductivity in polyelectrolyte hydrogels. *Macromolecules* **2016**, *49*, 9239−9246.

(28) Feng, Y. H.; Zhang, X. P.; Hao, Y. Y.; Ren, G. Y.; Guo, X. D. Simulation study of the pH sensitive directed self-assembly of rheins for sustained drug release hydrogel. *Colloids Surf., B* **2020**, *195*, 111260.

(29) Liu, Z.; Basem, A.; Mostafa, L.; Jasim, D. J.; Al-Rubaye, A. H.; Salahshour, S.; Hekmatifar, M.; Esmaeili, S. Investigating the effect of pH on the swelling process, mechanical and thermal attributes of polyacrylamide hydrogel structure: A molecular dynamics study. *Case Stud. Therm. Eng.* **2024**, *55*, 104148.

(30) De, S.; Aluru, N.; Johnson, B.; Crone, W.; Beebe, D.; Moore, J. Equilibrium swelling and kinetics of pH-responsive hydrogels: models, experiments, and simulations. *Journal of Microelectromechanical Systems* **2002**, *11*, 544−555.

(31) Dai, S.; Ravi, P.; Tam, K. C. pH-responsive polymers: synthesis, properties and applications. *Soft Matter* **2008**, *4*, 435−449.

(32) Ahn, S.-k.; Kasi, R. M.; Kim, S.-C.; Sharma, N.; Zhou, Y. Stimuli-responsive polymer gels. *Soft Matter* **2008**, *4*, 1151−1157.

(33) Saraydın, D.; Işıkver, Y. Calculations of the magnitude of responsivities in pH-, temperature-, and ion-responsive hydrogels. *Mater. Today Commun.* **2022**, *31*, 103253.

(34) Gao, K.; Xu, K. Advancements and Prospects of pH-Responsive Hydrogels in Biomedicine. *Gels* **2025**, *11*, 293.

(35) Tanaka, T.; Fillmore, D. J. Kinetics of swelling of gels. *J. Chem. Phys.* **1979**, *70*, 1214−1218.

(36) Keidel, R.; Ghavami, A.; Lugo, D. M.; Lotze, G.; Virtanen, O.; Beumers, P.; Pedersen, J. S.; Bardow, A.; Winkler, R. G.; Richtering, W. Time-resolved structural evolution during the collapse of responsive hydrogels: The microgel-to-particle transition. *Sci. Adv.* **2018**, *4*, No. eaao7086.

(37) Dallari, F.; Lokteva, I.; Möller, J.; Roseker, W.; Goy, C.; Westermeier, F.; Boesenberg, U.; Hallmann, J.; Rodriguez-Fernandez, A.; Scholz, M.; et al. Real-time swelling-collapse kinetics of nanogels driven by XFEL pulses. *Sci. Adv.* **2024**, *10*, No. eadm7876.

(38) Zhou, W.; Yang, G.; Ni, X.; Diao, S.; Xie, C.; Fan, Q. Recent advances in crosslinked nanogel for multimodal imaging and cancer therapy. *Polymers* **2020**, *12*, 1902.

(39) Wang, H.; Gao, L.; Fan, T.; Zhang, C.; Zhang, B.; Al-Hartomy, O. A.; Al-Ghamdi, A.; Wageh, S.; Qiu, M.; Zhang, H. Strategic design of intelligent-responsive nanogel carriers for cancer therapy. *ACS Appl. Mater. Interfaces* **2021**, *13*, 54621−54647.

(40) Zhao, J.; Su, H.; Vansuch, G. E.; Liu, Z.; Salaita, K.; Dyer, R. B. Localized nanoscale heating leads to ultrafast hydrogel volume-phase transition. *ACS Nano* **2019**, *13*, 515−525.

(41) Park, C. S.; Kang, Y.-W.; Na, H.; Sun, J.-Y. Hydrogels for bioinspired soft robots. *Prog. Polym. Sci.* **2024**, *150*, 101791.

(42) Podgornik, R. General theory of charge regulation and surface differential capacitance. *J. Chem. Phys.* **2018**, *149*, 104701.

(43) Murmiliuk, A.; Košovan, P.; Janata, M.; Procházka, K.; Uhlík, F.; Štěpánek, M. Local pH and effective p K of a polyelectrolyte chain: Two names for one quantity? *ACS Macro Lett.* **2018**, *7*, 1243−1247.

(44) Curk, T. Dissipative particle dynamics for coarse-grained models. *J. Chem. Phys.* **2024**, *160*, 174115.

(45) Park, N.; Kim, J. Hydrogel-based artificial muscles: Overview and recent progress. *Adv. Intell. Syst.* **2020**, *2*, 1900135.

(46) Ilmain, F.; Tanaka, T.; Kokufuta, E. Volume transition in a gel driven by hydrogen bonding. *Nature* **1991**, *349*, 400−401.

(47) Jha, P. K.; Zwanikken, J. W.; Detcheverry, F. A.; de Pablo, J. J.; Olvera de la Cruz, M. Study of volume phase transitions in polymeric nanogels by theoretically informed coarse-grained simulations. *Soft Matt* **2011**, *7*, 5965−5975.

(48) Park, T. G.; Hoffman, A. S. Synthesis and characterization of pH-and/or temperature-sensitive hydrogels. *J. Appl. Polym. Sci.* **1992**, *46*, 659−671.

(49) Kang, S. I.; Bae, Y. H. pH-Induced volume-phase transition of hydrogels containing sulfonamide side group by reversible crystal formation. *Macromolecules* **2001**, *34*, 8173−8178.

(50) Ni, H.; Kawaguchi, H.; Endo, T. Characteristics of pH-sensitive hydrogel microsphere of poly (acrylamide-co-methacrylic acid) with sharp pH−volume transition. *Colloid Polym. Sci.* **2007**, *285*, 873−879.

(51) Quesada-Pérez, M.; Maroto-Centeno, J. A.; Forcada, J.; Hidalgo-Alvarez, R. Gel swelling theories: the classical formalism and recent approaches. *Soft Matt* **2011**, *7*, 10536−10547.

(52) Yan, Q.; de Pablo, J. J. Monte Carlo simulation of a coarse-grained model of polyelectrolyte networks. *Phys. Rev. Lett.* **2003**, *91*, 018301.

(53) Raphael, E.; Joanny, J.-F. Annealed and quenched polyelectrolytes. *Europhys. Lett.* **1990**, *13*, 623.

(54) Uyaver, S.; Seidel, C. First-order conformational transition of annealed polyelectrolytes in a poor solvent. *Europhys. Lett.* **2003**, *64*, 536.

(55) Kazakov, A. D.; Prokacheva, V. M.; Rud, O. V.; Nová, L.; Uhlík, F. Modeling the phase transition in hydrophobic weak polyelectrolyte gels under compression. *Gels* **2023**, *9*, 259.

(56) He, J.; Zhou, Q.; Ge, Z.; Jiang, S.; Li, J.; Feng, W.; Yang, H. pH-gated switch of LCST-UCST phase transition of hydrogels. *Adv. Funct. Mater.* **2024**, *34*, 2404341.

(57) Nürnberg, H. W. The determination of the rate constants of dissociation and recombination for carboxylic acids by high level Faradaic rectification. *Z. Chem. Anal.* **1966**, 149.

(58) Sano, T.; Yasunaga, T. Kinetic studies of dissociation and recombination reaction in aqueous solutions of dicarboxylic acids by means of ultrasonic absorption measurements. *J. Phys. Chem.* **1973**, *77*, 2031−2038.

(59) Kanzaki, Y.; Tokuda, K.; Bruckenstein, S. Dissociation rates of weak acids using sinusoidal hydrodynamic modulated rotating disk electrode employing Koutecky-Levich equation. *J. Electrochem. Soc.* **2014**, *161*, 770−779.

(60) Ranatunga, K. Temperature dependence of mechanical power output in mammalian (rat) skeletal muscle. *Exp. Physiol.* **1998**, *83*, 371−376.

(61) Mirfakhrai, T.; Madden, J. D.; Baughman, R. H. Polymer artificial muscles. *Mater. Today* **2007**, *10*, 30−38.

(62) Kim, Y. S.; Liu, M.; Ishida, Y.; Ebina, Y.; Osada, M.; Sasaki, T.; Hikima, T.; Takata, M.; Aida, T. Thermoresponsive actuation enabled by permittivity switching in an electrostatically anisotropic hydrogel. *Nat. Mater.* **2015**, *14*, 1002−1007.

(63) Ma, Y.; Hua, M.; Wu, S.; Du, Y.; Pei, X.; Zhu, X.; Zhou, F.; He, X. Bioinspired high-power-density strong contractile hydrogel by programmable elastic recoil. *Sci. Adv.* **2020**, *6*, No. eabd2520.

(64) Safi Samghabadi, F.; Ramezani Bajgiran, S.; Villegas Orellana, M.; Conrad, J. C.; Marciel, A. B. Charge state of weak polyelectrolyte brushes determines salt-dependent swelling and hysteretic behavior. *ACS Macro Lett.* **2024**, *13*, 1570−1576.

(65) Yuan, J.; Tanaka, H. Impact of Hydrodynamic Interactions on the Collapse-Expansion Kinetics of Nanogels. *Macromolecules* **2024**, *57*, 10861−10869.

(66) Ko, J.; Kim, C.; Kim, D.; Song, Y.; Lee, S.; Yeom, B.; Huh, J.; Han, S.; Kang, D.; Koh, J.-S.; Cho, J. High-performance electrified hydrogel actuators based on wrinkled nanomembrane electrodes for untethered insect-scale soft aquabots. *Science Robotics* **2022**, *7*, No. eabo6463.

(67) Ko, J.; Kim, D.; Song, Y.; Lee, S.; Kwon, M.; Han, S.; Kang, D.; Kim, Y.; Huh, J.; Koh, J.-S.; et al. Electroosmosis-driven hydrogel actuators using hydrophobic/hydrophilic layer-by-layer assembly-induced crack electrodes. *ACS Nano* **2020**, *14*, 11906−11918.

(68) Eichenbaum, G. M.; Kiser, P. F.; Simon, S. A.; Needham, D. pH and ion-triggered volume response of anionic hydrogel microspheres. *Macromolecules* **1998**, *31*, 5084−5093.

(69) Landsgesell, J.; Hebbeker, P.; Rud, O.; Lunkad, R.; Košovan, P.; Holm, C. Grand-Reaction Method for Simulations of Ionization Equilibria Coupled to Ion Partitioning. *Macromolecules* **2020**, *53*, 3007−3020.

(70) Hockney, R. W.; Eastwood, J. W. *Computer Simulation Using Particles*; IOP Publishing: Bristol, 1988.

(71) Kikuchi, N.; Ryder, J. F.; Pooley, C. M.; Yeomans, J. M. Kinetics of the polymer collapse transition: The role of hydrodynamics. *Phys. Rev. E* **2005**, *71*, 061804.

(72) Manghi, M.; Schlagberger, X.; Kim, Y.-W.; Netz, R. R. Hydrodynamic effects in driven soft matter. *Soft Matt* **2006**, *2*, 653−668.

(73) Yuan, J.; Tanaka, H. Hydrodynamic effects on the collapse kinetics of flexible polyelectrolytes. *Phys. Rev. Lett.* **2024**, *132*, 038101.

(74) Yuan, J.; Curk, T. Collapse and expansion kinetics of a single polyelectrolyte chain with hydrodynamic interactions. *J. Chem. Phys.* **2024**, *160*, na.

(75) Groot, R. D.; Warren, P. B. Dissipative particle dynamics: Bridging the gap between atomistic and mesoscopic simulation. *J. Chem. Phys.* **1997**, *107*, 4423−4435.

(76) Thompson, A. P.; Aktulga, H. M.; Berger, R.; Bolintineanu, D. S.; Brown, W. M.; Crozier, P. S.; in 't Veld, P. J.; Kohlmeyer, A.; Moore, S. G.; Nguyen, T. D.; Shan, R.; Stevens, M. J.; Tranchida, J.; Trott, C.; Plimpton, S. J. LAMMPS - a flexible simulation tool for particle-based materials modeling at the atomic, meso, and continuum scales. *Comput. Phys. Commun.* **2022**, *271*, 108171.

(77) Laio, A.; Parrinello, M. Escaping free-energy minima. *Proc. Natl. Acad. Sci. U.S.A.* **2002**, *99*, 12562−12566.

(78) Fiorin, G.; Klein, M. L.; Hénin, J. Using collective variables to drive molecular dynamics simulations. *Mol. Phys.* **2013**, *111*, 3345−3362.

(79) Van Der Vegt, N. F.; Haldrup, K.; Roke, S.; Zheng, J.; Lund, M.; Bakker, H. J. Water-mediated ion pairing: Occurrence and relevance. *Chem. Rev.* **2016**, *116*, 7626−7641.

(80) Shi, R.; Cooper, A. J.; Tanaka, H. Impact of hierarchical water dipole orderings on the dynamics of aqueous salt solutions. *Nature Comm.* **2023**, *14*, 4616.

(81) Rafique, M.; Erbaş, A. Mechanical deformation affects the counterion condensation in highly-swollen polyelectrolyte hydrogels. *Soft Matter* **2023**, *19*, 7550−7561.

(82) Nguyen, M.; Rick, S. W. The influence of polarizability and charge transfer on specific ion effects in the dynamics of aqueous salt solutions. *J. Chem. Phys.* **2018**, *148*, na.

(83) Israelachvili, J. N. *Intermolecular and Surface Forces*, 3rd ed.; Academic: San Diego, 2011.

(84) Korevaar, P. A.; Kaplan, C. N.; Grinthal, A.; Rust, R. M.; Aizenberg, J. Non-equilibrium signal integration in hydrogels. *Nature Comm.* **2020**, *11*, 386.

(85) Katke, C.; Korevaar, P. A.; Kaplan, C. N. Diffusiophoretic fast swelling of chemically responsive hydrogels. *Phys. Rev. Lett.* **2024**, *132*, 208201.